Static Field Correction in 2D and 3D Echo-Planar Imaging (EPI) Sequences

Josef Pfeuffer, Thorsten Feiweier, Heiko Meyer

Application Development, Siemens Healthineers AG, Erlangen, Germany

Objectives

- Provide background on sources of off-resonance-induced image distortions in Echo-Planar Imaging (EPI) sequences and discuss correction strategies.
- Demonstrate application of corrections in the product (2D-EPI) and in research packages[1] (3D-EPI, 3D GRadient-And-Spin-Echo, and 3D Arterial Spin Labeling).

The data presented in this article apply research sequences[1] and scanner inline reconstructions conducted at 3 Tesla with software version *syngo* MR XA60, utilizing the 3T MR scanner MAGNETOM Vida. The article focuses on the application of 2D Echo-Planar Imaging (2D-EPI), 3D Echo-Planar Imaging (3D-EPI), and 3D arterial spin labeling/3D gradient- and spin-echo (3D-ASL/3D-GRASE) sequences. For ASL postprocessing, the research package "*syngo*.via Frontier MR Arterial Spin Labeling (ASL) Perfusion Analysis[1]" was used.

Introduction

Fast imaging techniques, such as echo-planar imaging or spiral imaging, are sensitive to both static and dynamic perturbations of off-resonances in the magnetic field due to the long readout. These off-resonances stem from the presence of air-tissue interfaces in the magnetic field or from changing physiology like respiration [1, 2], and become more relevant at higher field strengths like 3T or 7T.

To address static off-resonances, a process of field homogenization known as "shimming" is employed. This routine optimizes the B_0 field specifically for the area of interest, minimizing static off-resonances. Shimming is limited by the number of available correction coils, usually designed to counteract large-scale field variations. However, despite shimming, fast imaging sequences are still susceptible to remaining off-resonances, particularly due to the intense local field distortions caused by air-tissue interfaces [3].

Dynamic off-resonances, primarily induced by respiration, contribute to variations in the resonance frequency also within the brain region over time, even when the subject's head remains stationary [4]. These phase variations, which evolve linearly over time, result from the respiratory-driven movement of organs in the thoracic and abdominal cavities, as well as changes in the oxygenation state of the respired gas.

In single-shot Echo Planar Imaging (EPI), changes in resonance frequency result in spatial shifts of voxel positions, primarily along the phase-encode direction [4]. Conversely, in spiral imaging, these frequency changes lead to time-varying blurring, resulting in either case in increased time-series noise [2]. In segmented acquisitions, frequency shifts may also induce ghosting artifacts.

For EPI imaging, the pixel shift in the phase encode (*y*) direction can be approximated as $\Delta y/p \approx \Delta f\, T_{acq}$, where *p* represents the pixel size, *f* is the frequency shift, and T_{acq} is the duration of the *k*-space readout. In the case of spiral imaging, significant sidelobes in the blurring point response function become apparent when the ratio *r/p* is approximately $2\, \Delta f\, T_{acq} > 1$, where *r* is the radius [5].

To address static off-resonance conditions caused by local variations in magnetic susceptibility, various geometric distortion correction methods have been developed [1, 3, 6–9]. Additionally, corrections have been implemented using the phase information of navigator echoes to compensate for magnetic field drift [2, 10].

Various postprocessing techniques have been employed, particularly in EPI-based structural, functional (fMRI), and diffusion MRI. Notably, distortion correction methods involve the use of fieldmaps, such as "FUGUE" from FSL at the Wellcome Center for Integrative Neuroimaging, Oxford, UK, or the "FieldMap toolbox" in SPM at the Functional Imaging Laboratory (FIL), UCL Queen Square Institute of Neurology, London, UK.

FUGUE in FSL serves as a comprehensive set of tools for correcting distortions in EPI images. It addresses functional-image distortion due to magnetic field inhomo-

---

[1]*The research application is currently under development and is not for sale in the U.S. and in other countries. Its future availability cannot be ensured.*

geneities, particularly at air-bone or air-tissue interfaces in the sinuses. These inhomogeneities result in geometric distortion and signal loss, notably in the inferior frontal and temporal regions. Field inhomogeneities are quantified using a fieldmap, and the measured field values enable the calculation of geometric distortion and signal loss. This information is then utilized to compensate for, though not entirely eliminate, these artifacts. Compensation is achieved by geometrically unwarping the EPI images and applying cost-function masking in registrations to disregard areas affected by signal loss. It is crucial to emphasize that post-processing cannot restore regions where signal loss has occurred, as the signal loss is permanent. The only viable approach to recover signal in these areas is through the utilization of alternative acquisition techniques [3, 11].

Likewise, the SPM toolbox is crafted to generate fieldmaps following reference [1]. Studies have demonstrated that applying this method for distortion correction leads to enhanced geometric alignment between EPI and anatomical images [12].

In recent updates of the *syngo*.MR product from Siemens Healthineers, a new feature called "Static Field Correction" has been introduced for 2D-EPI sequences, including BOLD, diffusion, and perfusion sequences. When selected in the user interface of the sequence protocol, this option initiates an inline adjustment process. It involves shimming and measuring an absolute B0 map over a broader area of interest, which is then interpolated to the specific slices utilized in the target application protocol. This information is incorporated into the 2D and 3D distortion correction postprocessing, allowing for the

unwarping and correction of EPI distortions [13, 14]. Besides shifting image information to spatially accurate locations, this includes a brightness correction which compensates for the corresponding change of pixel density.

Furthermore, in the research package illustrated below, this method has been extended to 3D sequences such as 3D-EPI and 3D-ASL. This expansion ensures that the benefits of static field correction are now applicable to a wider range of imaging sequences, contributing to improved distortion correction in both 2D and 3D contexts.

Magnetic field inhomogeneities and distortions

The source of distortion in an EPI readout is caused by magnetic field inhomogeneities and by the low bandwidth in the phase-encode direction of the EPI sampling scheme.

Figure 1 illustrates the EPI sampling scheme in both the readout (RO) and phase-encode (PE) directions. A segmented *k*-space sampling is depicted for an EPI factor of five, indicating five lines are acquired per excitation (1A). The sampling scheme is further illustrated in the time domain (1B), featuring RO and PE gradients with corresponding sampling points. Filled dots represent one line of sampling in the PE direction, where the sampling distance is notably larger compared to the RO sampling. As a result, the bandwidth in the PE direction (BandwidthInPhaseEncode, BW_{PE}) is considerably smaller than the bandwidth in the RO direction (BW_{RO}), typically differing by one to two orders of magnitude.
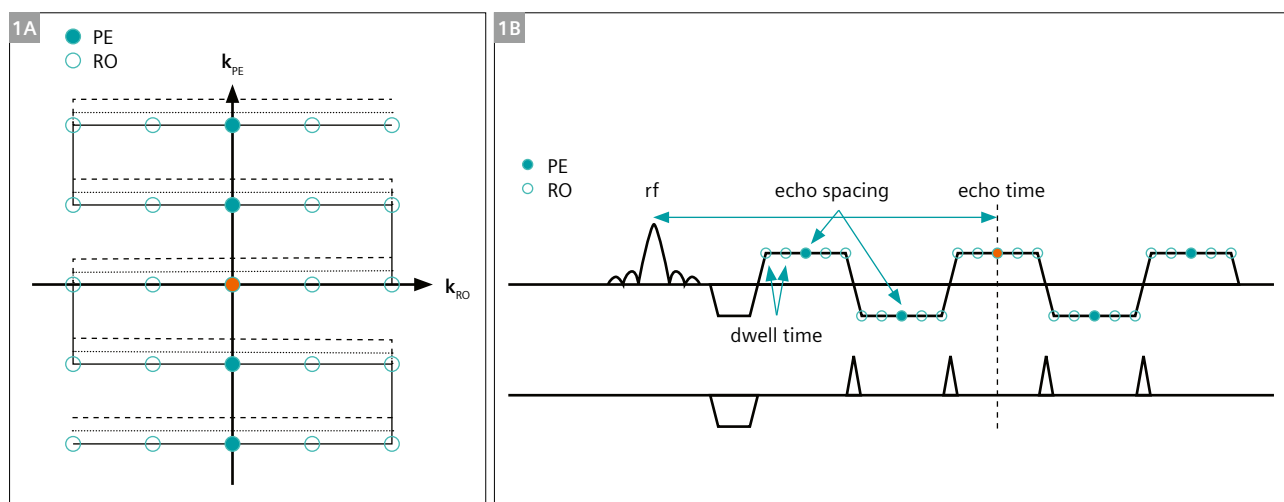
1 EPI sampling scheme in both the readout (RO) and phase-encode (PE) directions. **(1A)** A segmented *k*-space sampling is depicted for an EPI factor of five, meaning five lines acquired per excitation. **(1B)** The sampling scheme is further illustrated in the time domain, featuring RO and PE gradients with corresponding sampling points. Filled dots represent sampling in the PE direction, where the sampling distance (echo spacing) is notably larger compared to the RO sampling (dwell time). As a result, the bandwidth in the PE direction (BandwidthInPhaseEncode, BW_{PE}) is considerably smaller than the bandwidth in the RO direction (BW_{RO}), typically differing by one to two orders of magnitude.

As mentioned before, one way of correcting these distortions is to use a fieldmap to first quantify the amount of displacement and signal change.

A fieldmap can be acquired with a dual or triple gradient-echo sequence. The calculation of an absolute fieldmap – which is required for this type of correction – requires proper consideration of additional chemical shift-related phase evolutions and potential phase wraps [15–18]. It is calculated from the phase difference map $\Delta\phi$ into a field map, i.e., B_0 field variations ΔB_0 using:

$$\Delta B_0 \ [Hz] = \Delta\phi \ / \ (2\pi \ \Delta TE)$$

The pixel shift Δy in phase-encode direction is then given by:

$$\Delta y = \Delta B_0 \ / \ BW_{PE}$$

Figure 2 depicts the correlation between the fieldmap in Hz and the displacement in the phase-encode (PE) direction in mm. This relationship is determined by the Bandwidth-InPhaseEncode (BW_{PE}), which is specified in this example as 12 Hz/mm from data shown in Figure 3. Local off-resonances in the brain at 3T, for example in the frontal lobe or ear canals, can be up to 100 Hz.

To illustrate this, consider a voxel with a field offset of 48 Hz. The corresponding displacement can be calculated as 48 Hz divided by 12 Hz/mm, resulting in a 4 mm displacement. To enhance clarity, the displacement map is discretized in 1 mm increments, revealing contour lines that represent equal displacements.

A calculation of BW_{PE} involves the number of interleaves (for segmented EPI) and the PAT acceleration:

$$EffectiveEchoSpacing = \frac{EchoSpacing}{(NumInterleaves \times PatFactor)}$$

$$BW_{PE} \ [Hz/mm] \approx (FOV \times EffectiveEchoSpacing)^{-1}$$

Another often-used definition of BW_{PE} is given in units of Hz/Px. Hereby, the actual interpolation into the target image matrix has to be considered while taking into account phase oversampling, phase resolution, and the interpolated phase resolution. It can be approximated by:

$$BW_{PE} \ [Hz/Px] \approx \\ (BaseRes \times InterpolFactor \times EffectiveEchoSpacing)^{-1}$$

In the single-shot EPI example from Figure 3, BW_{RO} is 1144 Hz/Px, esp 960 µs, PAT factor 3, FOV 256 mm, base resolution 208, interpolation factor 2:

$$EffectiveEchoSpacing = \frac{esp \ 960 \ \mu s}{PAT \ 3} = 320 \ \mu s$$

$$BW_{PE} \ [Hz/mm] \approx (256 \ mm \times 320 \ \mu s)^{-1} = 12 \ Hz/mm$$

Note that phase partial Fourier and echo time are not contained in this formula and do not affect BW_{PE} and thus distortions. Also, expanding from the commonly used product 2D-EPI to 3D-EPI, z-encoding in 3D-EPI does not change or influence the "in-plane" distortion in the phase-encode direction, since a new excitation takes place in between segments.

Fat-water shift in EPI

Chemical-shift artifacts are minimal in the frequency-encode direction but may be large in the phase-encode direction. The reason for this difference is again the low BW_{PE}. EPI protocols thus typically suppress lipid signal to avoid overlapping water and fat contributions from different spatial positions in the image.
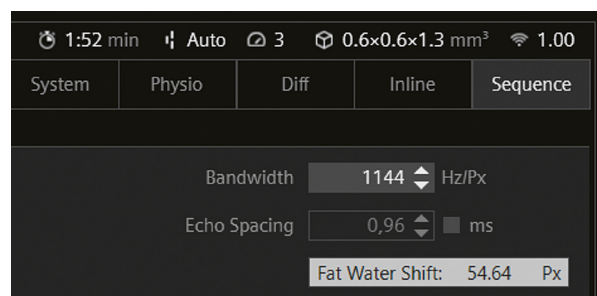

The fat-water shift of 3.3 ppm is 407 Hz (at 3T) in frequency units. The EPI sequence UI tooltip of "Echo Spacing" shows the fat-water shift in Px units, from which the BW_{PE} can be calculated:

$$BW_{PE} \ [Hz/Px] = \frac{Fat\text{-}Water \ Shift \ [Hz]}{Fat\text{-}Water \ Shift \ [Px]}$$

For the example single-shot EPI protocol from Figure 3, outlined in the text, the tooltip shows a fat-water shift of 54.64 Px. This results in:

$$BW_{PE} \ [Hz/Px] \approx \frac{407 \ Hz}{54.64 \ Px} = 7.4 \ Hz/Px$$

$$BW_{PE} \ [Hz/mm] \approx \\ 7.4 \ Hz/Px \times 208 \ Px \times \frac{2}{256 \ mm} = 12 \ Hz/mm$$
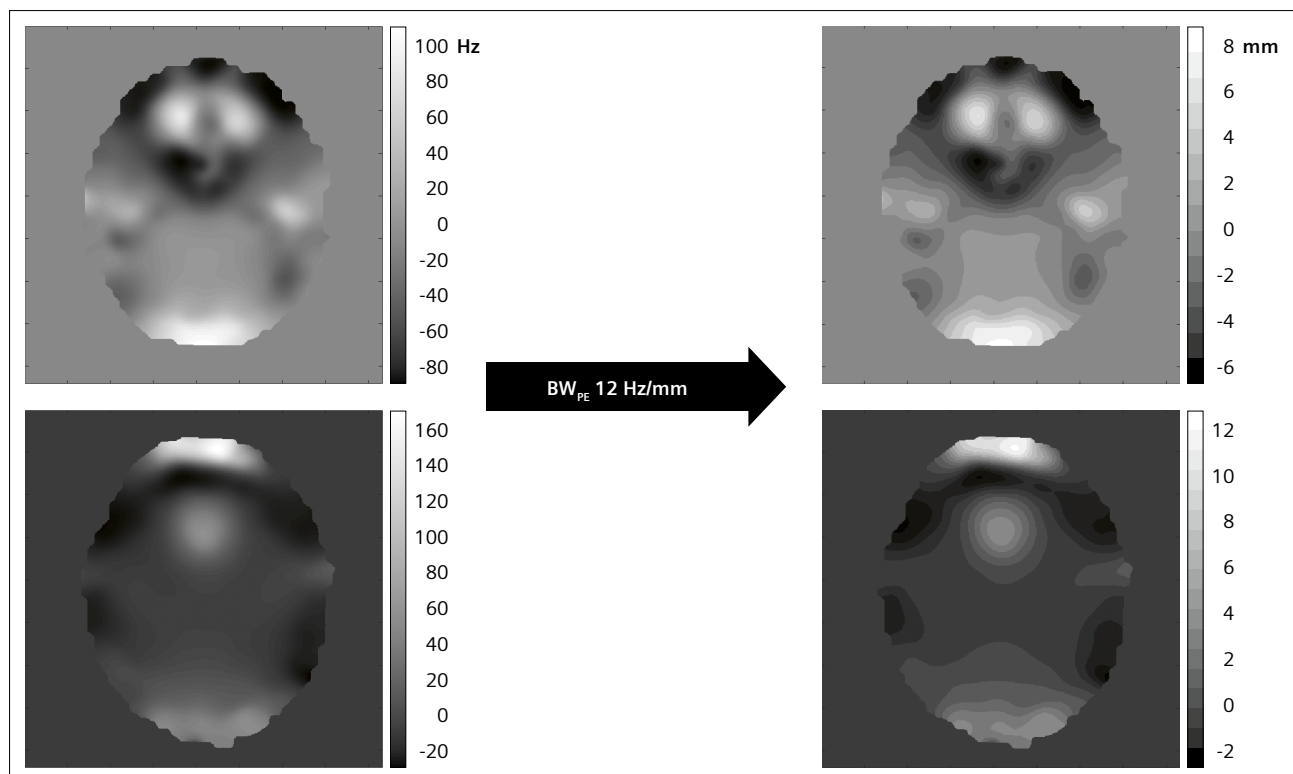
2 Correlation between the fieldmap in Hz and the displacement in the phase-encode (PE) direction in mm (contour lines: 1 mm) shown for two slices (inferior (top), superior (bottom)). This relationship is determined by the BW_{PE} of 12 Hz/mm. The top row slice is derived from the images showcased in Figure 3.
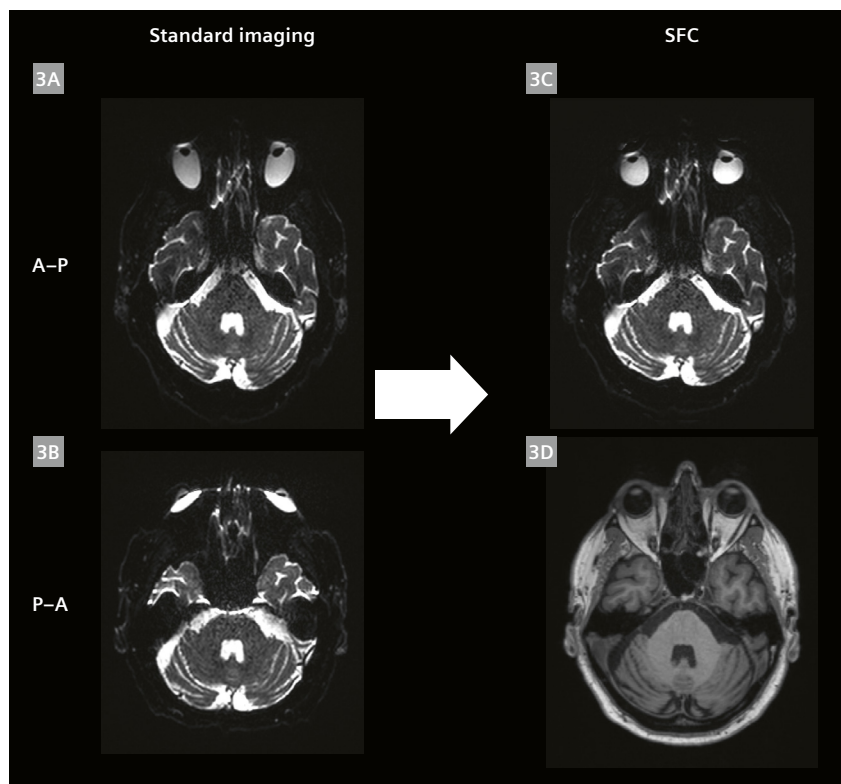
3 Distortions and correction in 2D-Spin-Echo-Echo-Planar Imaging (2D-SE-EPI). **(3A, 3B)** Alternating the phase-encode direction from anterior-posterior (A–P) to posterior-anterior (P–A) results in a sign inversion of distortions – stretching instead of compressions and vice versa. Utilizing a computed voxel displacement map, a less distorted representation **(3C)** that closely aligns with the anatomical reference MPRAGE **(3D)** can be created.

Imaging parameters:
2D-SE-EPI: FOV 256 × 256 mm², 100 slices, resolution 0.62 × 0.62 × 1.3 mm³ (interpolated), TE 81 ms, TR 18.4 s, BW_{RO} 1144 Hz/Px, esp 0.96 ms, BW_{PE} 7.4 Hz/Px (12 Hz/mm), PAT 3, EF 70, TA 1:52 min.

For sequences from Siemens Healthineers, the information about BW_{PE} is stored in the DICOM header with the parameter "Bandwidth Per Pixel Phase Encode", in DICOM tags (0019, 1028), and (0021, 1153) for the software platforms *syngo* MR Numaris 4 and Numaris X, respectively.

In summary, what influences distortions as given by BW_{PE} (Hz/mm) for EPI protocols?

• The echo spacing, which changes with readout bandwidth and readout resolution, i.e., FOV and matrix.
• The PAT acceleration and number of interleaves (for segmented EPI).

In contrast, when phase partial Fourier is used and thus also the minimum echo time is reduced, distortions in EPI are not affected or reduced. Also, reducing the echo time alone does not affect the distortions, only the T2* contrast and image SNR. The number of EPI distortions is solely determined by the (effective) echo spacing, i.e., how fast neighboring *k*-space *lines* are acquired.

Example of EPI distortion correction for 2D-SE-EPI

Figure 3 investigates distortions and correction in 2D Spin-Echo Echo-Planar Imaging (2D-SE-EPI). Subfigures 3A and 3B illustrate the impact of alternating the phase-encode direction from anterior-posterior (A–P) to posterior-anterior (P–A), resulting in a sign inversion of distortions – stretching instead of compressions and vice versa. By leveraging the measured ΔB_0 field and sampling speed in the phase-encode direction, as depicted in Figure 2, a voxel displacement map in the phase-encode direction can be computed. This map is then utilized to correct the image, producing a less distorted representation that closely aligns with the anatomical reference MPRAGE, as indicated in subfigures 3C and 3D.

It is crucial to note that the protocol settings were intentionally set to values highlighting large distortions for demonstration purposes. In typical clinical protocols, distortions are smaller.
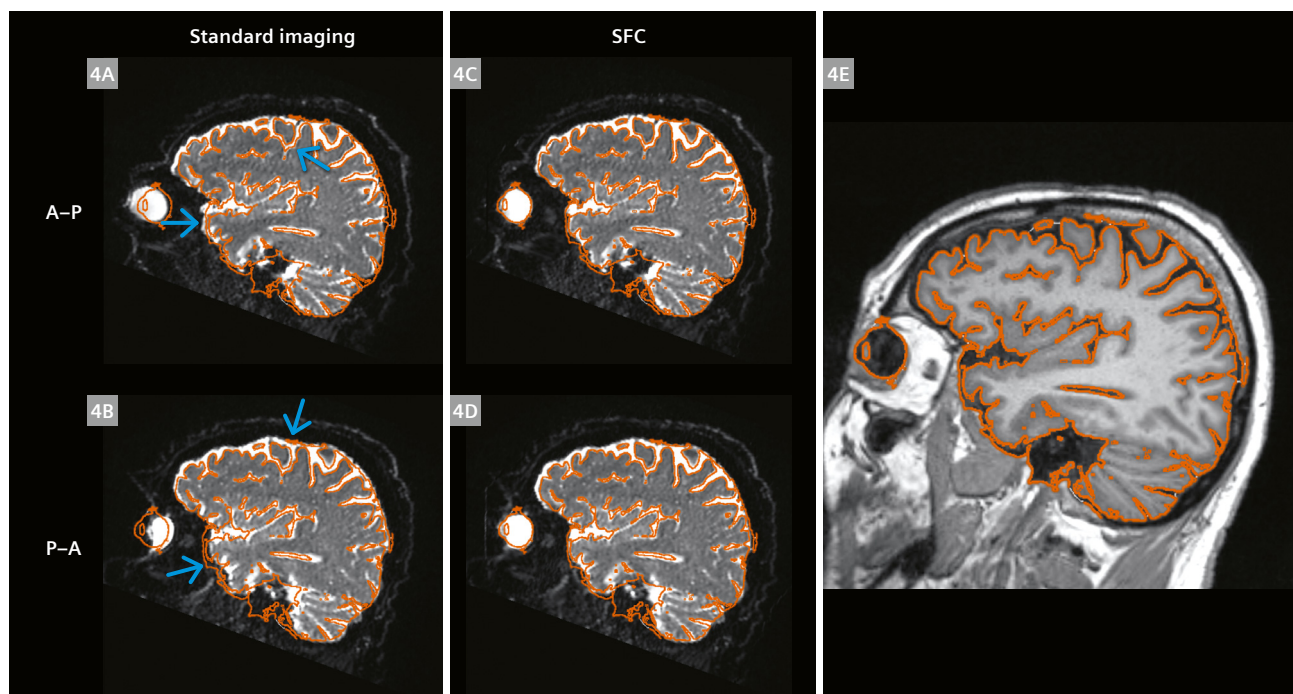
4 A sagittal reformat of 2D-SE-EPI. **(4E)** shows an MPRAGE image as the anatomical reference. A contour (in orange) outlines the geometry of the boundary between gray matter and cerebrospinal fluid (CSF). **(4A, 4B)** highlight distortions in images acquired with anterior-posterior (A–P) and posterior-anterior (P–A) phase-encoding directions, respectively, in standard imaging. Regions with geometrical mismatches become evident (red arrows). **(4C, 4D)** show the same data applying static field correction, demonstrating the improved spatial alignment with the reference image.

Imaging parameters: same 2D-SE-EPI data as shown in Figure 3.

Figure 4 illustrates distortions and corrections on a sagittal reformat of the same 2D-SE-EPI data. On the right, the anatomical reference is presented using MPRAGE imaging. A contour (in orange) outlines the geometry of the boundary between gray matter and cerebrospinal fluid (CSF). The left column highlights distortions in images acquired with anterior-posterior (A–P) and posterior-anterior (P–A) phase-encoding directions, respectively, before correction. By overlaying the anatomical contour, regions with geometrical mismatches become evident. The middle column shows the same data after applying the static field correction, demonstrating the improved spatial alignment with the reference image.

Static Field Correction (SFC) for 3D Echo-Planar-Imaging (3D-EPI)

Protocol parameters for the 3D-EPI example were selected to align more closely with a clinical use case, emphasizing reduced sensitivity to distortions. This is evident in the higher BW_{PE} value of 35 Hz/mm, in contrast to the 12 Hz/mm used in the previous example for demonstration purposes.

Figure 5 displays two slices acquired using the 3D-EPI sequence. The first image is standard imaging (5A), while the second image shows Static Field Correction (SFC) (5B). For comparison, a virtually "distortion-free" 3D gradient-echo sequence is depicted (5C).

Additionally, a displacement map with contour lines at 0.5 mm is provided to outline the spatial location of the distortions (5D). The displacement map reveals minimal shifts in the upper (cranial) slices and within the brain. However, more substantial shifts are evident in the nasal areas, frontal lobe, and eye bulbs. This visualization underscores the impact of static field correction in reducing distortions in the 3D-EPI sequence, particularly in regions prone to significant shifts.
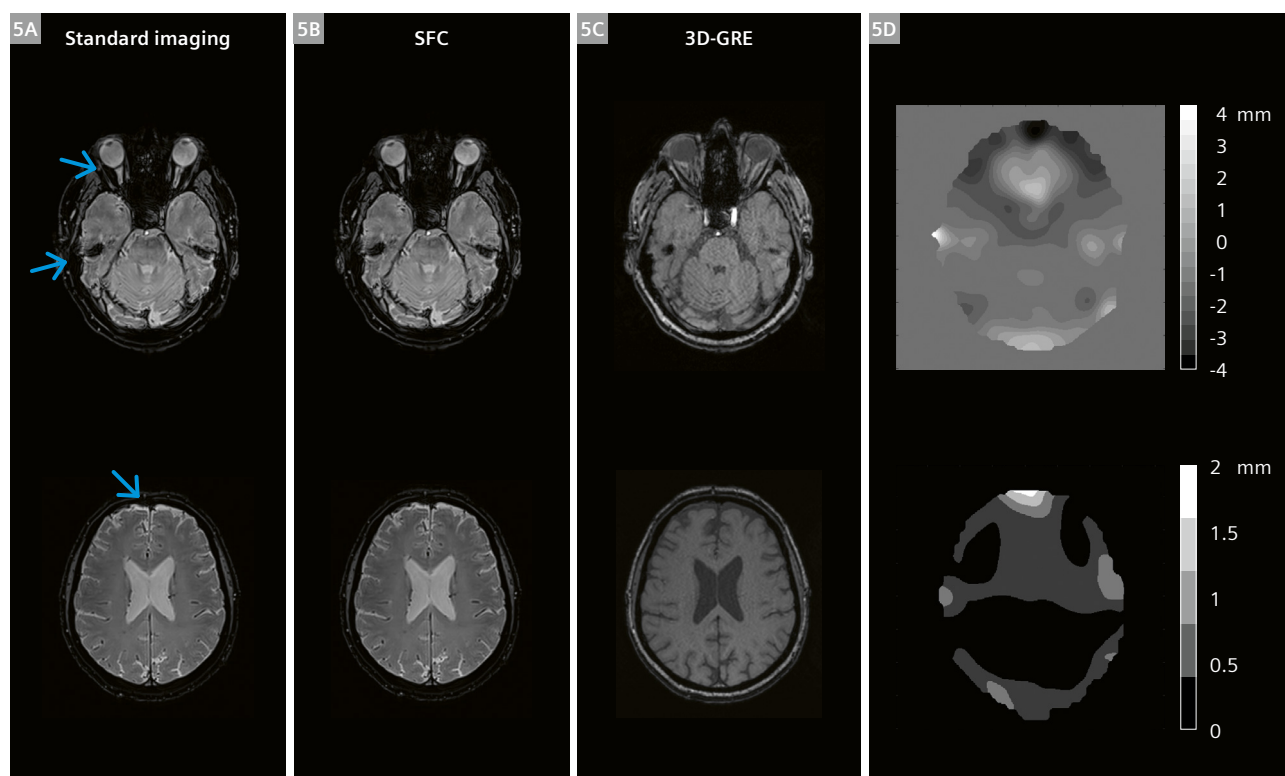
5 Two slices acquired using the 3D-EPI sequence, with standard imaging **(5A)** and with Static Field Correction (SFC) **(5B)**. In comparison, a virtually "distortion-free" 3D gradient-echo sequence is displayed in **(5C)**. **(5D)** shows a displacement map in mm with contour lines at 0.5 mm. The displacement map reveals minimal shifts in the upper (cranial) slices and within the brain. However, significant larger shifts are observed in the nasal areas, frontal lobe, and eye bulbs (blue arrows).

Imaging parameters: 3D-EPI, FOV 256 × 256 mm², 112 slices, resolution 0.62 × 0.62 × 1.3 mm³ (interpolated), TE 23 ms, TR 58 ms, FA 10°, BW_{RO} 422 Hz/Px, esp 2.62 ms, BW_{PE} 21.2 Hz/Px (34.5 Hz/mm), PAT 2, EF 9, seg 12, TA 1:20 min.

SFC for 3D-GRASE and 3D-Arterial Spin Labeling (ASL)

Figure 6 displays the 3D-GRASE imaging from the 3D-ASL sequence, specifically the M0 image with ASL labeling switched off, both with standard imaging and with static field correction. An anatomical MPRAGE image of the same slice is presented in 6D. The displacement map, with contour lines at 0.5 mm, indicates minimal shifts within the brain but significant shifts in the nasal areas and eyeballs. In this ASL protocol with an isotropic resolution of 3 mm, the echo spacing was 0.54 ms and the BW_{PE} value was 39 Hz/mm. These parameter choices contribute to the fine spatial detail of the acquisition and to its reduced sensitivity to distortions, aligning with the requirements for ASL imaging.

With SFC applied, the distortion in the eyeball is shifted back, as indicated by the arrows, resulting in a distortion that is now closer to the anatomical "true" object size.
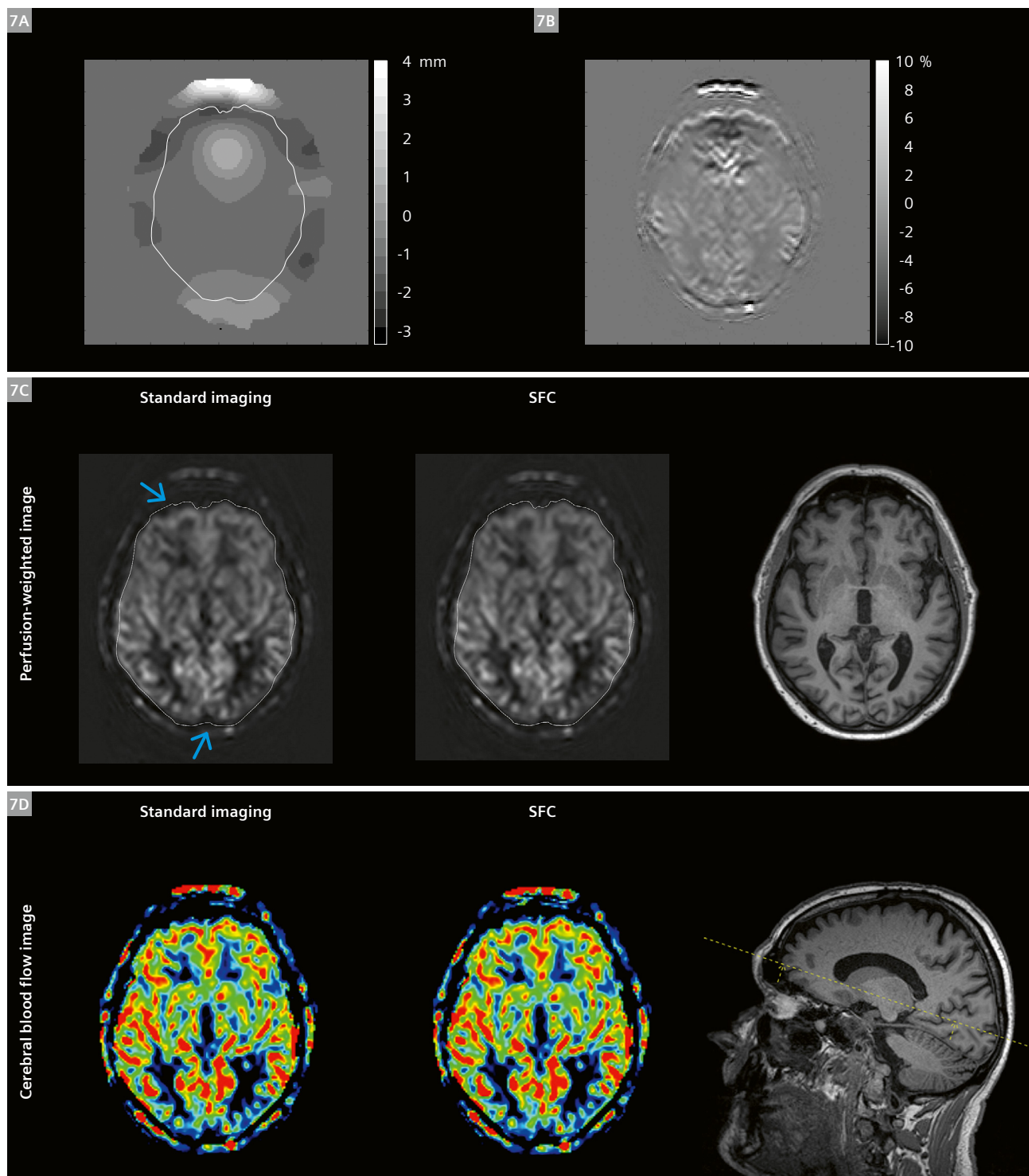
In the context of arterial spin labeling (ASL) imaging, we applied the same imaging parameters as we did in the 3D-GRASE sequence. The labeling duration for pseudo-continuous ASL (PCASL) and the post-labeling delay were set at 1800 ms each. Our study involved a 71-year-old male subject, and Figure 7 showcases the 3D-ASL imaging results.
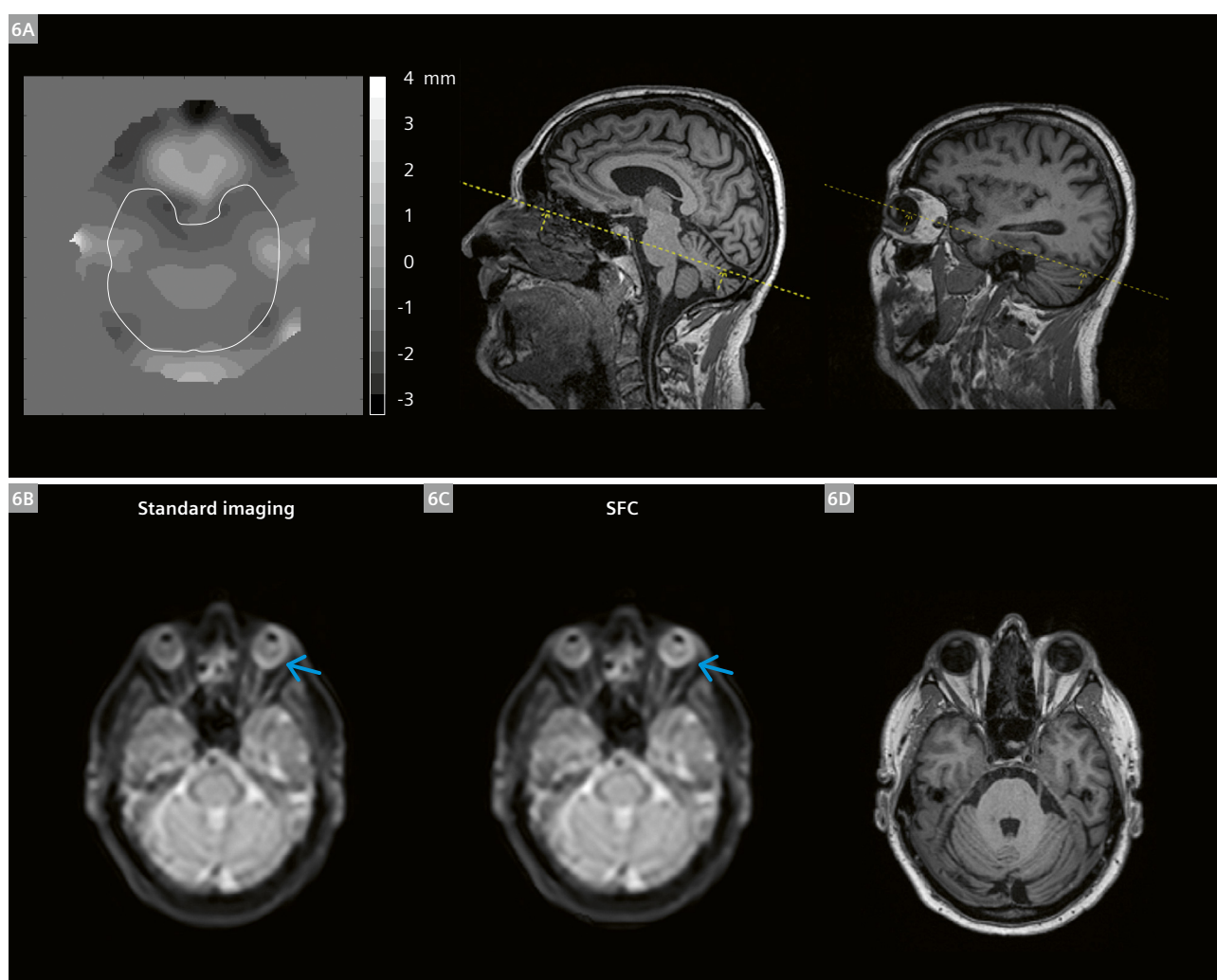
6 3D-GRASE image of the 3D-ASL sequence (M0 image, ASL labeling switched off) before and after SFC **(6B, 6C)**. Anatomical MPRAGE image of the same slice **(6D)**. Displacement map (contour lines at 0.5 mm) **(6A)** indicates little shifts within the brain, but significant shifts in the nasal areas and eye bulbs.
With SFC, the eyeball distortion is shifted back as indicated by the arrows, now being similar to the anatomical "true" object size.

Imaging parameters: 3D-GRASE, FOV 256 × 256 mm², 42 slices, resolution 1.5 × 1.5 × 3.0 mm³ (interpolated), PAT 2, TE 14 ms, TR 4100 ms, FA 90/160°, BW_{RO} 2380 Hz/Px, esp 0.54 ms, BW_{PE} 58.8 Hz/Px (38.6 Hz/mm), TF 26, EF 15, seg 6, rep 1, TA 0:28 min.

7 Arterial Spin Labeling (ASL) imaging on a 71-year-old male subject using the 3D-ASL GRASE technique. The first and second columns present standard images and images with SFC, while the third column displays anatomical MPRAGE images for reference. Perfusion-weighted (PWI) and cerebral blood flow (relCBF) images are detailed in rows **(7C)** and **(7D)**, respectively.
The displacement map with contour lines set at 0.5 mm **(7A)** highlights the most significant displacements in the frontal and posterior regions, visualized as stretches and compressions. Intensity changes are effectively visible in the difference image of the perfusion-weighted image (in percent) standard and with SFC **(7B)**.

Same imaging parameters as in Figure 6: with PCASL labeling duration (LD) 1800 ms, post-labeling delay (PLD) 1800 ms, background suppression, number of repetitions 8, TA 7:12 min.

The first and second columns of Figure 7 depict standard images and images with SFC. For reference, the third column displays anatomical MPRAGE images. Rows 7C and 7D provide details on perfusion-weighted (PWI) and Cerebral Blood Flow (relCBF) images, respectively.

The displacement map, featuring contour lines set at 0.5 mm (7A), emphasizes notable displacements in the frontal and posterior regions, visually represented as stretches and compressions. Changes in intensity are effectively observed in the percent difference image of the PWI after the SFC (7B). Note the close similarity of
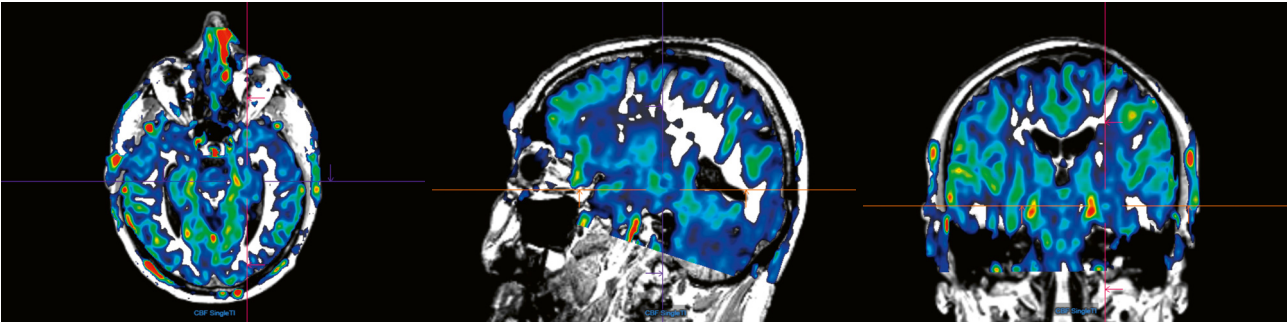
8 ASL imaging on a 71-year-old male subject using the 3D-ASL GRASE technique. The overlay of the cerebral blood flow map (relCBF) demonstrates excellent agreement with the anatomical gray-matter/white-matter (GM/WM) contrast.
Same imaging parameters as in Figure 7.
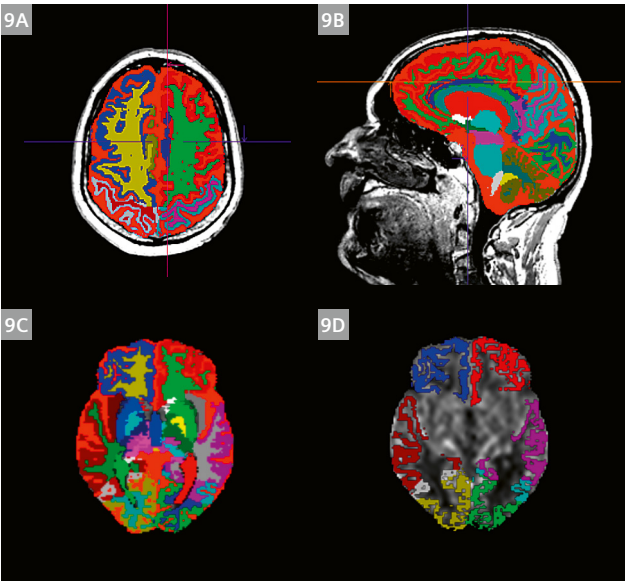
9 ASL imaging on a 71-year-old male subject using the 3D-ASL GRASE technique. Using a postprocessing research package, gray-matter/white-matter segmentation of anatomical structures was conducted utilizing an age-dependent atlas. **(9A, 9B, 9C)** exhibit all morphological regions across the entire brain, each depicted in distinct colors. **(9D)** selects a subset of regions, specifically highlighting the gray matter, in a given slice, superimposed on the cerebral blood flow (relCBF) image.

GM statistics relCBF [mL/(100 g min)], mean ± std				
	substructure right GM		substructure left GM	
	Standard	with SFC	Standard	with SFC
Total GM	33.1 ± 13.4	33.3 ± 13.3	33.3 ± 13.2	33.5 ± 13.0
Occipital GM	28.3 ± 14.4	28.7 ± 14.0	28.2 ± 14.1	28.6 ± 13.9
Parietal GM	34.7 ± 13.0	34.9 ± 12.9	33.9 ± 13.5	34.1 ± 13.4
Frontal GM	36.3 ± 11.2	36.6 ± 11.0	37.5 ± 11.5	37.7 ± 11.3
Temporal GM	34.3 ± 14.3	34.4 ± 14.2	31.9 ± 14.0	32.1 ± 13.8
Cerebellum GM	22.9 ± 9.6	23.1 ± 9.6	25.3 ± 8.4	25.5 ± 8.4

Table 1: Cerebral Blood Flow (relCBF) values with standard imaging and after static field correction (SFC). Following gray-matter (GM) partial volume analysis, an automated statistical analysis of morphologically labeled regions across the entire brain was generated.
After applying SFC, the mean relCBF values notably increased, accompanied by a reduction in standard deviation across all gray-matter regions. This improvement can be attributed to the enhanced alignment of the CBF map with the anatomical image in gray-matter pixels.

spatial features in the displacement map and the PWI percent change map.

The 3D-ASL images in Figure 8 show the overlay of the cerebral blood flow map (relCBF), demonstrating excellent agreement with the anatomical gray-matter/white-matter (GM/WM) contrast. This showcases the effectiveness of the correction techniques in achieving accurate and reliable imaging results.

Utilizing a postprocessing research package, morphological analysis was conducted, specifically gray-matter/white-matter segmentation of anatomical structures. Subfigures 9A, 9B, and 9C display morphological regions across the entire brain, each represented in distinct colors. Subfigure 9D selects a subset of regions, specifically highlighting the gray matter, in a given slice, superimposed on the relCBF image.

The table presents cerebral blood flow values after SFC. Following gray-matter partial volume analysis, an automated statistical analysis of morphologically labeled regions across the entire brain was generated.

Following SFC, there was a notable increase in mean relCBF values, accompanied by a reduction in standard deviation across all gray-matter regions. This improvement can be attributed to the enhanced alignment of the CBF map with the anatomical image in gray matter pixels.

SFC applied to 3D-ASL sequences effectively reduces distortions in anatomical structures, particularly in regions prone to significant shifts, resulting in improved alignment of cerebral blood flow (relCBF) maps with anatomical images, and increased accuracy in gray-matter segmentation, as demonstrated in a 3 mm isotropic resolution protocol.

Conclusions

In conclusion, this article addresses the challenges posed by magnetic field inhomogeneities and distortions in fast imaging techniques like echo-planar imaging. Methods to mitigate distortions include shimming, fieldmap acquisition and geometric distortion correction. The introduction of the "Static Field Correction" feature in the Syngo MR product, initially for 2D-EPI sequences and here extended to 3D research sequences, demonstrates significant benefits of distortion correction. The impact of distortions in both 2D and 3D sequences is illustrated through examples, emphasizing the efficacy of SFC. The article further explores the influence of BW_{PE} on distortions in EPI protocols, providing a comprehensive understanding of the factors affecting image quality. Finally, the application of SFC in 3D-ASL sequences is highlighted, showcasing its effectiveness in improving cerebral blood flow mapping and automated reporting using gray-matter segmentation. Overall, the study contributes valuable insights into distortion correction techniques and their impact on imaging quality in various MRI sequences.

References

1 Jezzard P, Balaban RS. Correction for geometric distortion in echo planar images from B0 field variations. Magn Reson Med. 1995;34(1):65–73.
2 Pfeuffer J, Van de Moortele PF, Ugurbil K, Hu X, Glover GH. Correction of physiologically induced global off-resonance effects in dynamic echo-planar and spiral functional imaging. Magn Reson Med. 2002;47(2):344–353.
3 Andersson JL, Skare S, Ashburner J. How to correct susceptibility distortions in spin-echo echo-planar images: application to diffusion tensor imaging. Neuroimage. 2003;20(2):870–888.
4 Raj D, Paley DP, Anderson AW, Kennan RP, Gore JC. A model for susceptibility artefacts from respiration in functional echo-planar magnetic resonance imaging. Phys Med Biol. 2000;45(12):3809–3820.
5 Glover GH, Lai S. Self-navigated spiral fMRI: interleaved versus single-shot. Magn Reson Med. 1998;39(3):361–368.
6 Noll DC, Pauly JM, Meyer CH, Nishimura DG, Macovski A. Deblurring for non-2D Fourier transform magnetic resonance imaging. Magn Reson Med. 1992;25(2):319–333.
7 Irarrazabal P, Meyer CH, Nishimura DG, Macovski A. Inhomogeneity correction using an estimated linear fieldmap. Magn Reson Med 1996;35(2):278–282.
8 Andersson JL, Hutton C, Ashburner J, Turner R, Friston K. Modeling geometric deformations in EPI time series. Neuroimage. 2001;13(5):903–919.
9 Durand E, Van De Moortele PF, Pachot-Clouard M, Le Bihan D. Artifact due to B(0) fluctuations in fMRI: correction using the *k*-space central line. Magn Reson Med. 2001;46(1):198–201.
10 Liu HL, Kochunov P, Lancaster JL, Fox PT, Gao JH. Comparison of navigator echo and centroid corrections of image displacement induced by static magnetic field drift on echo planar functional MRI. J Magn Reson Imaging. 2001;13(2):308–312.

11 Holland D, Kuperman JM, Dale AM. Efficient correction of inhomogeneous static magnetic field-induced distortion in Echo Planar Imaging. Neuroimage. 2010;50(1):175–183.

12 Hutton C, Bork A, Josephs O, Deichmann R, Ashburner J, Turner R. Image distortion correction in fMRI: A quantitative evaluation. Neuroimage. 2002;16(1):217–240.

13 Tong A, Lemberskiy G, Huang C, Shanbhogue K, Feiweier T, Rosenkrantz AB. Exploratory study of geometric distortion correction of prostate diffusion-weighted imaging using B0 map acquisition. J Magn Reson Imaging. 2019;50(5):1614–1619.

14 Graunhan NF, Grünebach N, Brockstedt L, Sanner A, Feiweier T, Schöffling V, et al. Reduction of Distortion Artifacts in Brain MRI Using a Field Map-based Correction Technique in Diffusion-weighted Imaging: A Prospective Study. Clin Neuroradiol. 2023. doi: 10.1007/s00062-023-01338-3. Epub ahead of print.

15 Dagher J, Reese T, Bilgin A. High-resolution, large dynamic range field map estimation. Magn Reson Med. 2014;71(1):105–117.

16 Fautz HP, Gross P, Gumbrecht R. Method and computer to determine a B0 field map with a magnetic resonance apparatus. United States patent US 20150077115A1. 2015.

17 Gumbrecht R, Koehler M, Schneider R. Method and magnetic resonance apparatus for correction of a B0 map for chemical shifts. United States patent US 9830711B2. 2015.

18 Bredfeldt JS, Miao X, Kaza E, Schneider M, Requardt M, Feiweier T, et al. Patient specific distortion detection and mitigation in MR images used for stereotactic radiosurgery. Phys Med Biol. 2022;67(6):10.1088/1361-6560/ac508e.

19 Jin J, Tourell M, Sati P, Patil S, Liu K, Derbyshire J, et al. Segmented 3D EPI with CAIPIRINHA for Fast, High-Resolution T2*-weighted Imaging. Proceedings ISMRM 2021.

20 Jin J, O'Brien K, et al. Fast, High-resolution Whole Brain SWI and QSM with CAIPIRINHA 3D-EPI and Deep Learning Reconstruction. Proceedings ISMRM 2024.

Contact

Dr. Josef Pfeuffer
Siemens Healthineers AG
SHS DI MR RCT CLS NEUR
Erlangen
Germany
josef.pfeuffer@siemens-healthineers.com

Josef Pfeuffer   Thorsten Feiweier   Heiko Meyer